Pulsed-Field-Ionization Zero-Kinetic-Energy (PFI-ZEKE) Photoelectron Spectroscopic Study of the Renner−Teller Effect in the $\tilde{A}^+\ ^2\Pi$ State of OCS^+ †

M. Sommavilla and F. Merkt*

Physical Chemistry, ETH Zurich, CH-8093 Zurich, Switzerland

Received: May 19, 2004; In Final Form: July 20, 2004

The pulsed-field-ionization zero-kinetic-energy (PFI-ZEKE) photoelectron spectrum of OCS in a cold supersonic expansion has been measured in the region of the $\tilde{X}\ ^1\Sigma^+ \rightarrow \tilde{A}^+\ ^2\Pi$ and $\tilde{X}\ ^1\Sigma^+ \rightarrow \tilde{B}^+\ ^2\Sigma^+$ bands between 122 500 and 129 500 cm^{-1}. The spectrum of the $\tilde{X} \rightarrow A^+$ transition consists of extensive and strongly perturbed vibrational progressions in the CO- and CS-stretching modes ν_3 and ν_1, respectively. The perturbations, which arise from Fermi interactions between CS-stretching and bending levels, are revealed by (i) the observation of several members of the bending progression, (ii) the very irregular spacings between the two spin−orbit components of the stretching levels, and (iii) numerous anomalies in the vibrational intensity distribution. A complete analysis of the spectrum is presented that takes the spin−orbit interaction, the Renner−Teller effect, and Fermi interactions in the $\tilde{A}^+$ ionic state into account. This analysis provides a fully satisfactory explanation for the strongly perturbed positions of the vibrational levels of the $\tilde{A}^+$ state and for the anomalous intensity distribution of the photoelectron spectrum. The analysis also enabled the derivation of reliable information on the bending levels and of a set of spectroscopic parameters describing the Renner−Teller effect in the $\tilde{A}^+$ state of OCS^+. Two closely spaced strong lines have been observed near the origin of the $\tilde{X} \rightarrow \tilde{B}^+$ band. The upper one was assigned to the origin of the $\tilde{X} \rightarrow \tilde{B}^+$ transition by extrapolation of the autoionizing Rydberg series.

1. Introduction

The photoelectron spectra of CO_2, OCS, and CS_2 in the region of 10−20 eV have been extensively studied and compared.[1−15] Next to uncovering many features of the vibronic energy level structure of the first electronic states of the cations, these studies have contributed to highlight important aspects of the photoionization dynamics in these molecules. A comparison of the He I photoelectron spectra of the three molecules is presented, for example, in Figure 2 of ref 8. The photoelectron spectra are dominated by four bands corresponding to transitions from the $\tilde{X}\ ^1\Sigma^+_{(g)}$ neutral ground state to the $\tilde{X}^+\ ^2\Pi_{(g)}$, $\tilde{A}^+\ ^2\Pi_{(u)}$, $\tilde{B}^+\ ^2\Sigma^+_{(u)}$, and $\tilde{C}^+\ ^2\Sigma^+_{(g)}$ ionic states. These bands have represented an important source of information on the cations, which has complemented that obtained from optical spectra.[16−23]

The photoelectron spectra of CO_2, OCS, and CS_2 offer the means to study the Renner−Teller effect in molecular systems subject to both spin−orbit and Fermi interactions and to investigate how these interactions influence the photoionization dynamics. Photoelectron spectroscopic studies of these molecules have also been used to demonstrate the capabilities of new photoelectron spectrometers and techniques and to study fundamental aspects of molecular photoionization. Wang et al., for instance, demonstrated how rotational and Doppler broadening of photoelectron bands could be eliminated by recording the spectra of samples in cold supersonic expansions.[8] In their classical study of the threshold photoelectron spectrum of CO_2, Baer and Guyon[7] carefully analyzed the mechanisms that lead to the production of electrons of near-zero kinetic energy in the Franck−Condon gap between the $\tilde{X}^+\ ^2\Pi_g$ and $\tilde{A}^+\ ^2\Pi_u$ states of CO_2^+ and showed the importance of resonant autoionization,[24] which is a mechanism that is expected to be important in all polyatomic molecules.

Of all photoelectron bands in these systems, the $\tilde{X}\ ^1\Sigma^+ \rightarrow \tilde{A}^+\ ^2\Pi$ band of OCS is the least well-characterized. The band is extremely congested, and many details of the vibronic energy level structure of the $\tilde{A}^+$ state have not been fully extracted yet, not even in the latest high-resolution study by pulsed-field-ionization zero-kinetic-energy (PFI-ZEKE) photoelectron spectroscopy.[14] The dominance of the progressions in the stretching modes was already recognized in earlier studies.[1,2] Frey et al.,[3] Delwiche et al.,[4] and Potts and Fattahallah[5] were the first to partially resolve the spin−orbit doublets of the stretching levels and to obtain reliable estimates of the stretching frequencies and the spin−orbit coupling constant.

The determination of the bending frequency of the $\tilde{A}^+$ state of OCS^+ has turned out to be a challenge, because the excitation of bending levels has a very low intensity, as a result of vanishing Franck−Condon factors. Estimates in the range of 340−380 cm^{-1} could nevertheless be made on the basis of the position of the allowed 2^1_1 hot band.[5,6,8,14] These estimates differ from those that have been inferred from the attribution of weak features to transitions out of the ground neutral vibronic state to bending levels and range from 400 cm^{-1} (data taken from ref 8) to 590 cm^{-1} (data taken from ref 6). Generally, the bending frequency is difficult to determine, because the bending levels are split into several components by the Renner−Teller effect. For instance, the 2^1 level splits into four levels of symmetry $^2\Sigma^+$, $^2\Delta_{5/2}$, $^2\Delta_{3/2}$, and $^2\Sigma^-$, and it is not easy to extract the bending frequency from a partially resolved photoelectron spectrum. Only in high-resolution spectra can the spectral features be assigned unambiguously to members of the bending

† Part of the special issue "Tomas Baer Festschrift".

* Author to whom correspondence should be addressed. E-mail address: merkt@phys.chem.ethz.ch.

10.1021/jp0478458 CCC: $27.50
Published on Web 09/08/2004

progression, and Chen et al. have proposed many assignments of transitions to bending levels on the basis of the correspondence between level positions calculated ab initio and spectral features observed in the synchrotron PFI-ZEKE photoelectron spectrum.[14] However, the assignments often were no more than tentative.

The present study was motivated by our interest in the Renner−Teller effect and by the realization that the current knowledge of the $\tilde{X}\ ^1\Sigma^+ \rightarrow \tilde{A}^+\ ^2\Pi$ band of OCS, and particularly that of the bending levels of the $\tilde{A}^+$ state of OCS^+, could be advanced by a high-resolution photoelectron spectroscopic study. We exploit here an indirect source of information on the bending levels that becomes accessible when the resolution is sufficiently high that the perturbations of the stretching levels caused by Fermi interactions with the bending levels can be detected: A deperturbation analysis can then be used to characterize the bending levels.

Although the resolution of better than 0.1 cm^{-1}, which can now be attained by photoelectron spectroscopy,[25] would be sufficient to resolve the rotational structure in the photoelectron spectra of molecules with rotational constants comparable to that of the $\tilde{A}^+$ state of OCS^+, we have not concentrated on the rotational structure of the spectra. It is indeed known from optical spectra[20,22,23] and photoionization spectra[26] that all excited vibrational levels of the $\tilde{A}^+$ state of OCS^+ are predissociative and have a natural width larger than the spacing between the transitions to low rotational levels.

2. Experiment

The PFI-ZEKE photoelectron spectra have been recorded using a narrow-bandwidth VUV laser system that was coupled to a photoion/photoelectron time-of-flight mass spectrometer. The laser system and the photoelectron spectrometer have been described in refs 27 and 28, and only aspects specific to the present study are briefly summarized here.

VUV radiation in the range 122 000−129 000 cm^{-1} was generated by two-photon resonance-enhanced sum-frequency mixing ($\nu_{VUV} = 2\nu_1 + \nu_2$) in krypton using the $(4p)^5 5p[1/2]$ ($J = 0$) ← $(4p)^6\ ^1S_0$ two-photon resonance at $2\tilde{\nu}_1 = 94092.96\ cm^{-1}$. The VUV wavenumber was scanned by tuning the wavenumber $\tilde{\nu}_2$. Two dye lasers pumped by an injection-seeded Nd:YAG laser were used as input beams to the nonlinear frequency upconversion process, and, when necessary, their wavenumber was doubled and tripled in β-barium borate crystals. The VUV wavenumber was calibrated to an absolute accuracy of 0.5 cm^{-1} by measuring the laser-induced fluorescence spectra of molecular iodine and the optogalvanic spectra of argon and neon.

The photoelectron spectra were recorded by monitoring the pulsed-field ionization of high Rydberg states located just below the successive ionization thresholds as a function of the VUV laser wavenumber. Thus, the lines in these spectra correspond to energy differences between the vibronic states of the ion and the neutral ground state.

OCS was introduced into the spectrometer by means of a skimmed supersonic expansion of a mixture of argon and OCS (spectroscopic-grade purity) in a dilution ratio of 4:1. To avoid the formation of Ar^+ ions in the photoexcitation region, argon was replaced by neon as the inert gas in the expansion above the ionization potential of argon (127109.8 cm^{-1}). To measure the PFI-ZEKE photoelectron spectra, a sequence of two pulsed electric fields was used, with a first discrimination pulse of 70 mV/cm and a second detection pulse of −220 mV/cm. The pulse sequence was applied 5 μs after photoexcitation. The first pulse primarily served the purpose of eliminating electrons with nonzero kinetic energy, and the PFI-ZEKE photoelectron spectra were recorded by monitoring the electrons released by the second pulse.

The full width at half-maximum (fwhm) of the observed transitions amounted to ∼5 cm^{-1} and was determined by the unresolved rotational envelope of the vibrational bands (see above). The rapid decay of the vibrationally excited levels of the $\tilde{A}^+$ state of OCS^+ implies that dissociation of the ion core has already occurred when the pulsed electric field is applied and that the Rydberg electrons have remained attached to the S^+ fragments. The field-induced lowering of the ionization thresholds was taken into account by adding 1.5 cm^{-1} to the measured line positions, as estimated using the method described in ref 25.

Because of strong ionization into the ionization channels associated with the $\tilde{X}^+$ ionic ground state, the ion density in the photoexcitation region had to be monitored carefully and kept to a level of $<10^6$ ions/cm^3 to prevent artifacts associated with the formation of plasmalike conditions.[29] Under conditions where the ion density becomes too large, electrons emitted with low kinetic energy just above each threshold have a tendency to remain trapped in the ion cloud and become partially released when the pulsed electric field is applied, leading to an undesirable broadening of the lines on their high-wavenumber side. This potential artifact could be eliminated either by reducing the VUV laser intensity or by applying a discrimination pulse of sufficient amplitude and duration to eliminate all trapped electrons.

Photoionization spectra of OCS have also been recorded through the entire region between the $\tilde{A}^+$ and $\tilde{B}^+$ states. The ions were extracted with an electric field of 430 V/cm and accelerated toward a microchannel plate detector located at the end of a time-of-flight (TOF) tube. In this energy region, both OCS^+ and S^+ ions were produced by ionization and dissociative ionization, respectively. Spectra of the different ionic products (OCS^+, S^+) were obtained by placing temporal gates at the corresponding positions in the TOF spectrum. Monitoring these ions as a function of the VUV wavenumber led to the observation of several Rydberg series converging on the ground vibronic level of the $\tilde{B}^+$ state.

3. The Renner−Teller Effect in the $\tilde{A}^+\ ^2\Pi$ State of OCS^+

To model the vibrational energy level structure in the $\tilde{A}^+\ ^2\Pi$ state of OCS^+ and the intensity distribution in the photoelectron spectrum of the $\tilde{X} \rightarrow \tilde{A}^+$ transition, one must consider the Renner−Teller effect, the spin−orbit interaction, and Fermi interactions between stretching and bending levels simultaneously. The energy level structure of linear molecules in electronic states of $^2\Pi$ symmetry subject to these interactions has been discussed in general terms in refs 30 and 31. In CO_2, CO_2^+, CS_2, and CS_2^+, Fermi interactions can only occur between the bending and symmetric stretching levels for symmetry reasons. In OCS and OCS^+, Fermi interactions are possible, in principle, between the bending (ν_2) and both CO (ν_3) and CS (ν_1) stretching levels. However, in the $\tilde{A}^+$ state of OCS^+, the strong mismatch between the CO-stretching wavenumber (∼2000 cm^{-1}) and twice the bending wavenumber (∼700 cm^{-1}) renders the effects of the Fermi interactions between the bending and CO-stretching levels negligible. Therefore, we only consider here the Fermi interactions between the bending and CS-stretching levels.

The vibrational energy level structure of the $\tilde{A}^+$ state of OCS^+, as it was determined in the present study, is displayed in Figure 1. The figure gives an overview of the main

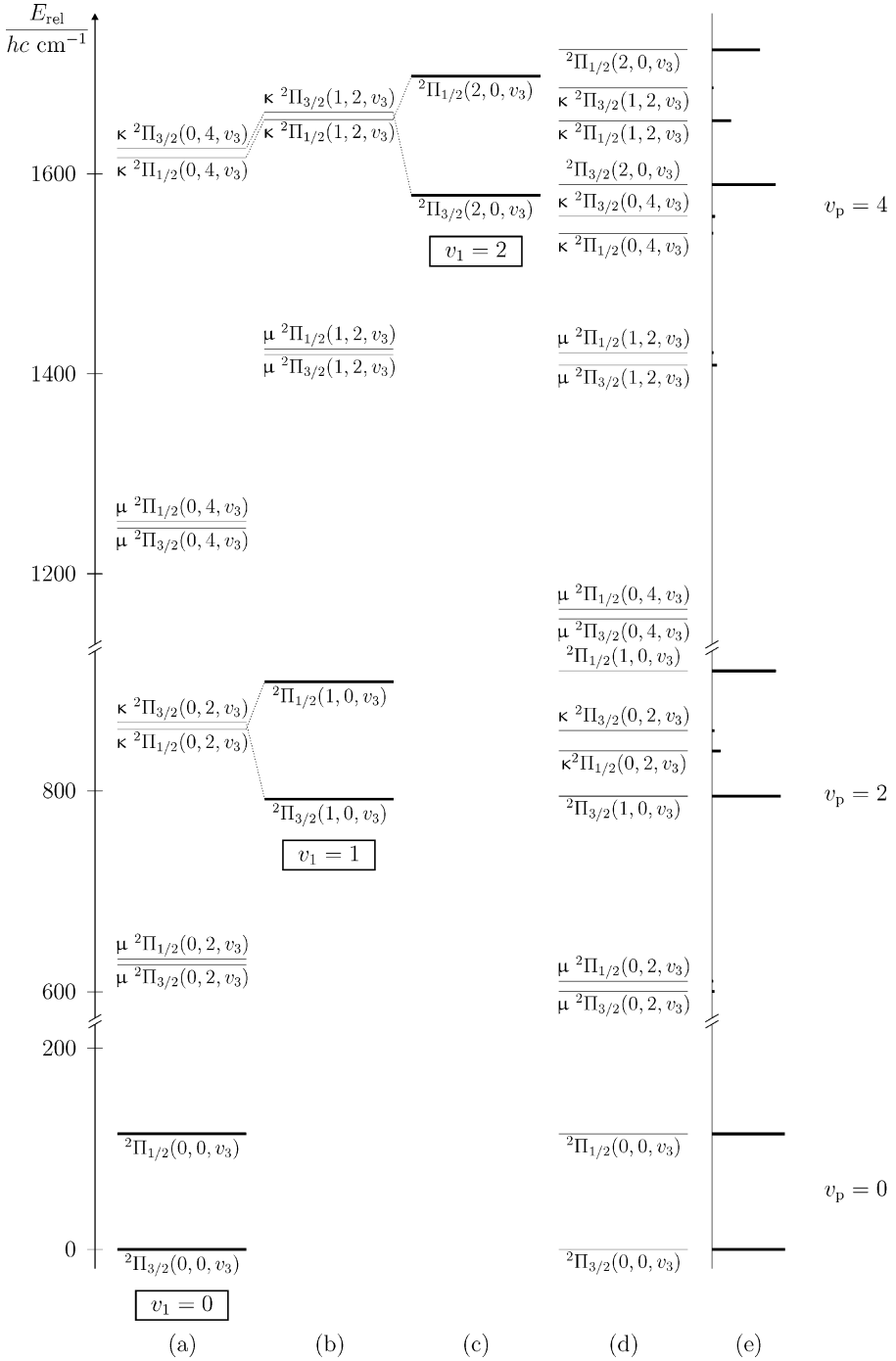

Figure 1. Overview of the energy level structure in the Fermi polyads with $v_p = 0$, 2, and 4 of the $\tilde{A}^+\ ^2\Pi$ state of OCS^+. The diagram corresponds to the result of the final analysis of the $v_3 = 1$ progression of the photoelectron spectrum but, here, serves the purpose of showing the main contributions to the energy level structure and to the spectral intensities. The first three columns (panels a−c) correspond to a calculation of the energies of CS-stretching levels indicated by the bold horizontal lines and bending levels associated with (a) $v_1 = 0$, (b) $v_1 = 1$, and (c) $v_1 = 2$, which neglect the effects of the Fermi interactions with the CS-stretching levels. When the Fermi interactions are considered, the energy level structure displayed in the fourth column (panel d) results. The last column (panel e) graphically represents the relative intensity distribution expected within each polyad for transitions out of the $\tilde{X}\ ^1\Sigma^+$ ground state of OCS, under the assumption that only transitions to the CS-stretching levels carry intensity. Under this assumption, only bending levels of Π symmetry ($|K| = 1$) can gain intensity in the photoelectron spectrum, and bending levels with $|K| \neq 1$ have been omitted from the figure, for simplicity. The labels μ and κ are the usual labels for levels corresponding to the lower and upper Renner−Teller potentials, respectively.

interactions between the bending and stretching levels that are relevant for the understanding of the photoelectron spectrum of the $\tilde{X} \rightarrow \tilde{A}^+$ transition and serves here primarily to illustrate the different contributions to the energy level structure and to explain how transitions to the bending levels of the $\tilde{A}^+$ state of OCS^+, which vanish in first approximation, gain intensity by Fermi interactions with the CS-stretching levels. The three columns on the left-hand side of Figure 1 indicate the "unperturbed" positions of the bending and CS-stretching levels expected for each progression associated with a given value of v_3 (the results displayed in the figure are for $v_3 = 1$).

Because the CS-stretching levels have Π vibronic symmetry, only bending levels of the Π vibronic symmetry can gain intensity by Fermi interactions. This implies that only bending levels associated with an even value of the polyad quantum number $v_p = 2v_1 + v_2$ (where v_1 and v_2 represent the vibrational

quantum number of the CS-stretching and bending levels, respectively) need to be considered, and that, within these polyads, all bending levels with Φ, H, ... vibronic symmetry are not observable in the photoelectron spectra. To avoid overloading the figure, only levels of Π vibronic symmetry have been retained. The Fermi interactions of the bending levels with the CS-stretching levels, which are indicated in bold in Figure 1, lead to the energy level structure displayed in the fourth column. The energy levels in this column correspond to eigenstates of mixed bending and CS-stretching character; however, only their dominant character is indicated in the figure. The CS-stretching characters of the eigenstates (calculated as described below) are represented by horizontal lines of varying length in the fifth column (panel e) of Figure 1, which, thus, gives an idea of the expected intensity distribution in the photoelectron spectrum. Not surprisingly, the transitions that are expected to have nonvanishing intensities in the photoelectron spectrum are clustered around the positions of the unperturbed CS-stretching levels.

The present analysis of the photoelectron spectrum of the $\tilde{X} \rightarrow \tilde{A}^+$ transition of OCS is based on the previous treatments of the Renner−Teller effect by Gauyacq and Jungen,[32] Brown and Jørgensen,[31] Frye and Sears,[19] and Smith et al.[33] These treatments rely on the diagonilization of an effective Hamiltonian matrix expressed in a finite basis set with basis functions:

$$|\Lambda,v_1\rangle|\Lambda,v_2,K\rangle|S,\Sigma\rangle \equiv |\Lambda,v_1,v_2,K,\Sigma\rangle \quad (1)$$

in which $|\Lambda,v_1\rangle$ and $|\Lambda,v_2,K\rangle$ represent the eigenfunctions of the harmonic oscillator with vibrational quantum numbers v_1 and v_2 for the CS-stretching and bending coordinates, respectively. Λ and Σ represent the quantum numbers associated with the projections of the electron orbital and spin angular momenta along the molecule axis, respectively, and $K = \Lambda + l$ corresponds to the projection quantum number resulting from the coupling of the orbital angular momentum and the vibrational angular momentum arising from the bending motion with quantum number $|l| \in \{v_2, v_2 - 2, v_2 - 4, ..., {}^1/_2(1 - (-1)^{v_2})\}$.

The Hamiltonian can be divided into five contributions:

$$\hat{H}_{\text{eff}} = \hat{H}_{\text{harm}} + \hat{H}_{\text{RT}} + \hat{H}_{\text{anharm}} + \hat{H}_{\text{Fermi}} + \hat{H}_{\text{SO}} \quad (2)$$

where the harmonic contribution $\hat{H}_{\text{harm}}$ represents a diagonal matrix with elements

$$\langle \pm 1,v_1,v_2,K,\Sigma|\hat{H}_{\text{harm}}| \pm 1,v_1,v_2,K,\Sigma\rangle = h\nu_1\left(v_1 + \frac{1}{2}\right) + h\nu_2(v_2 + 1) + h\nu_3\left(v_3 + \frac{1}{2}\right) \quad (3)$$

whereby the last term remains constant for the progressions in ν_1 and ν_2 analyzed here. The Renner−Teller Hamiltonian ($\hat{H}_{\text{RT}}$) leads to a removal of the electronic degeneracy for bending angles deviating from 180° and to two electronic potential curves—one with positive parity ($+,\Gamma_e = A'$ in C_s), the other with negative parity ($-,\Gamma_e = A''$ in C_s)—and its matrix elements are

$$\langle +1,v_1,v_2,K,\Sigma|\hat{H}_{\text{RT}}| -1,v_1,v_2,K,\Sigma\rangle = h\frac{\epsilon\nu_2}{2}\sqrt{a^2 - K^2} \quad (4)$$

$$\langle \pm 1,v_1,v_2,K,\Sigma|\hat{H}_{\text{RT}}| \mp 1,v_1,v_2 - 2,K,\Sigma\rangle = h\frac{\epsilon\nu_2}{4}\sqrt{(b \mp K)(a \mp K)} \quad (5)$$

where $a = \nu_2 + 1$ and $b = \nu_2 - 1$. ϵ represents the Renner parameter:

$$\epsilon = \frac{\phi_{22}^+ - \phi_{22}^-}{\phi_{22}^+ + \phi_{22}^-} \quad (6)$$

and can be expressed as a function of the harmonic force constants ϕ_{22}^+ and ϕ_{22}^- of the two bending potentials.

In $\Lambda = 0$ electronic states, the anharmonicity of the potential leads to the well-known expansion for the vibrational energies:

$$\frac{E_{\text{vib}}}{hc} = \frac{E_{\text{vib}}^{(\text{harm})}}{hc} + x_{11}\left(v_1 + \frac{1}{2}\right)^2 + x_{22}(v_2 + 1)^2 + x_{33}\left(v_3 + \frac{1}{2}\right)^2 + x_{12}\left(v_1 + \frac{1}{2}\right)(v_2 + 1) + x_{13}\left(v_1 + \frac{1}{2}\right)\left(v_3 + \frac{1}{2}\right) + x_{23}(v_2 + 1)\left(v_3 + \frac{1}{2}\right) + g_{22}l^2 \quad (7)$$

in which x_{ij} represents the anharmonicity constants and the term $g_{22}l^2$ removes the degeneracy of the bending levels.[30] In electronically degenerate states with $\Lambda \neq 0$, the anharmonicity associated with the bending motion must be treated separately: Whereas the pure bending anharmonicity leads to diagonal and off-diagonal elements coupling levels differing in v_2 by ±2 and ±4, according to the expressions listed in the upper half of Table 1 in ref 33, the stretch−bend anharmonicity leads to Fermi interactions between levels differing in v_1 by ±1 and in v_2 by ∓2, according to eqs 8−13 (see also the lower half of Table 1 in ref 33):

$$\langle \pm 1,v_1 + 1,v_2,K,\Sigma|\hat{H}_{\text{Fermi}}| \pm 1,v_1,v_2,K,\Sigma\rangle = 2W_1 a\sqrt{d} \quad (8)$$

$$\langle \pm 1,v_1 + 1,v_2,K,\Sigma|\hat{H}_{\text{Fermi}}| \mp 1,v_1,v_2,K,\Sigma\rangle = 2W_2\sqrt{d(a^2 - K^2)} \quad (9)$$

$$\langle \pm 1,v_1 + 1,v_2,K,\Sigma|\hat{H}_{\text{Fermi}}| \pm 1,v_1,v_2 - 2,K,\Sigma\rangle = W_1\sqrt{d(a \mp K)(b \pm K)} \quad (10)$$

$$\langle \pm 1,v_1 + 1,v_2,K,\Sigma|\hat{H}_{\text{Fermi}}| \mp 1,v_1,v_2 - 2,K,\Sigma\rangle = W_2\sqrt{d(a \mp K)(b \mp K)} \quad (11)$$

$$\langle \pm 1,v_1 + 1,v_2,K,\Sigma|\hat{H}_{\text{Fermi}}| \pm 1,v_1,v_2 + 2,K,\Sigma\rangle = W_1\sqrt{d(a \pm K)(e \mp K)} \quad (12)$$

$$\langle \pm 1,v_1 + 1,v_2,K,\Sigma|\hat{H}_{\text{Fermi}}| \mp 1,v_1,v_2 + 2,K,\Sigma\rangle = W_2\sqrt{d(a \pm K)(e \pm K)} \quad (13)$$

where $d = v_1 + 1$, $e = v_2 + 3$, and the Fermi interaction parameters W_1 and W_2 are functions of the cubic force constants ϕ_{122}^+ and ϕ_{122}^-:[34]

$$W_1 = \frac{1}{2}(\phi_{122}^+ + \phi_{122}^-) \quad (14)$$

$$W_2 = \frac{1}{2}(\phi_{122}^+ - \phi_{122}^-) \quad (15)$$

The spin−orbit interaction is taken into account by eq 16:

$$\langle \pm 1,v_1,v_2,K,\Sigma|\hat{H}_{\text{SO}}| \pm 1,v_1,v_2,K,\Sigma\rangle = \pm hcA_{\text{eff},v_1}\Sigma \quad (16)$$

in which the effective spin−orbit coupling constant A_{eff,v_1} is taken to be linearly dependent on the degree of excitation

in the CS-stretching mode:

$$A_{\mathrm{eff},\upsilon_1} = A_0 - \alpha_1 \upsilon_1 \tag{17}$$

Because of the predissociative nature of the vibrationally excited levels of the $\tilde{A}^+$ state and the associated width of $\sim$5 cm^{-1} of the observed lines in the PFI-ZEKE spectrum (see Section 4.1), the positions of the vibrational levels could not be determined accurately enough for the parameters describing the pure bending anharmonicity to be derived from our measurement. Consequently, only the Fermi interaction parameters W_1 and W_2 (eqs 8−15), the Renner parameter (eqs 4−6), the spin−orbit constants A_0 and α_1 (eqs 16 and 17), the harmonic wavenumbers (ω_1, ω_2, and ω_3), and the anharmonic coupling constants (x_{11}, x_{33}, x_{13}, and x_{23}) could be extracted from the experimental data. The anharmonic coupling constant x_{12} was found to be very small and, in addition, correlated to x_{11}; its value was set to zero in the analysis. Moreover, because of the structure of eq 7, rather than optimizing the harmonic constants ω_1, ω_2, and ω_3 in a nonlinear least-squares fit to the experimental data, it was more convenient to fit the constants

$$\omega_1^{(0)} = \omega_1 + \frac{1}{2}x_{13} \tag{18}$$

and

$$\omega_2^{(0)} = \omega_2 + \frac{1}{2}x_{23} \tag{19}$$

to the positions of the members of the progression associated with $\upsilon_3 = 0$, and fit the constants

$$\omega_1^{(1)} = \omega_1 + \frac{3}{2}x_{13} \tag{20}$$

and

$$\omega_2^{(1)} = \omega_2 + \frac{3}{2}x_{23} \tag{21}$$

to the positions of the members of the progression associated with $\upsilon_3 = 1$ (see Section 4.1). Similarly, the constants

$$\omega_3^{(0)} = \omega_3 + \frac{x_{13}}{2} + x_{23} \tag{22}$$

and x_{33} were extracted from the positions of the members of the $(0,0,\upsilon_3)$ progression. It was then straightforward to determine the constants ω_1, ω_2, ω_3, x_{13}, and x_{23}, using eqs 18−22.

The effective Hamiltonian approach to the treatment of the Renner−Teller effect in the photoelectron spectrum of the $\tilde{X} \rightarrow \tilde{A}^+$ band of OCS enables a simple treatment of the vibrational intensity distribution already outlined in the discussion of Figure 1: Because transitions to the bending levels are characterized by vanishing Franck−Condon factors, the intensity of transitions to these levels is entirely "borrowed" from transitions to CS-stretching levels that are in Fermi interaction with the bending levels. This intensity-borrowing mechanism implies that only the bending levels of Π symmetry can gain intensity, and that all other bending levels with $\Sigma^{\pm}$, Δ, Φ, Γ, etc. remain unobservable in the photoelectron spectrum of the $\tilde{X}\ ^1\Sigma^+ \rightarrow \tilde{A}^+\ ^2\Pi$ band of OCS, in accord with the experimental results (see Section 4).

The amount of stretching character of each bending level can be determined from the eigenvectors of $\hat{H}_{\mathrm{eff}}$ and used to simulate the intensity distribution of the photoelectron spectrum. Although one generally does not expect the intensity distribution in a PFI-ZEKE photoelectron spectrum to reflect the direct ionization cross-sections faithfully (see ref 35 for a general discussion), a calculation of the intensity distribution based on the assumption that the intensities correspond to direct-ionization cross sections provides a qualitative understanding of the mechanisms by which bending levels gain intensity and a means to confirm spectral assignments, as will be shown in the next section.

4. Results and Discussion

4.1. The PFI-ZEKE Photoelectron Spectrum of the $\tilde{X} \rightarrow \tilde{A}^+$ Band. An overview of the PFI-ZEKE photoelectron spectrum of OCS from the origin of the $\tilde{X} \rightarrow \tilde{A}^+$ band to the origin of the $\tilde{X} \rightarrow \tilde{B}^+$ band is displayed in Figure 2. The spectrum of the $\tilde{X} \rightarrow \tilde{A}^+$ band is composed of several vibrational progressions of the type $1_0^{\upsilon_1} 3_0^{\upsilon_3}$, with υ_1 ranging from 0 to 4 and υ_3 ranging from 0 to 3. The assignment of the progressions associated with $\upsilon_3 = 0-3$ are indicated along the assignment bars below the spectrum. The transitions to the vibrational levels of the $\tilde{A}^+$ state typically consist of doublets, separated by $\sim$120 cm^{-1}, corresponding to the two spin−orbit components of the $\tilde{A}^+\ ^2\Pi_\Omega$ state with $\Omega = {}^3/_2$ and ${}^1/_2$. The higher members of each progression in υ_1 with $\upsilon_1 \geq 1$ display more than two components, as a result of the Fermi interaction with the bending levels, as will be discussed in more detail below. The progressions with $\upsilon_3 \geq 2$ strongly overlap with the $\upsilon_3 = 0$ and 1 progressions above 127 000 cm^{-1}, and the spectrum in this region becomes too congested for unambiguous assignments to be made. For this reason, the analysis of the Renner−Teller effect presented below is restricted to the first two progressions with $\upsilon_3 = 0$ and 1 below 127 000 cm^{-1}. By far the most intense transitions in the spectrum are the two closely spaced lines located in the vicinity of the origin of the $\tilde{X} \rightarrow \tilde{B}^+$ transition at $\sim$129 350 cm^{-1}.

Even a cursory look at Figure 2 suffices to convey the impression that the spectrum of the $\tilde{X} \rightarrow \tilde{A}^+$ transition is perturbed. In Figures 3 and 4, the spin−orbit doublet of the first five bands of the $\upsilon_3 = 0$ and 1 progressions are compared on an expanded scale. To facilitate the comparison and highlight the irregularities, the positions of the lower spin−orbit components of the successive bands have been aligned: The spin−orbit splitting varies from band to band and weaker structures can be discerned in most bands with $\upsilon_1 \geq 1$. Both progressions display very similar irregularities. For instance, the $\upsilon_1 = 2$ component appears as a triplet in Figures 3c and 4c, and the $\upsilon_1 = 1$ and $\upsilon_1 = 2$ bands are characterized by particularly large splittings between the two main spin−orbit components.

The irregularities in the vibrational progressions can be accounted for quantitatively by considering the Fermi interactions between the stretching levels and the Renner−Teller components of the bending levels. To guide the assignment and obtain reliable information on the bending levels, an iterative procedure relying on calculations of the energy level structure, using the formalism outlined in Section 3, was followed, starting with the lowest Fermi polyads. In the lowest portion of the spectrum, only the Fermi coupling constants and the harmonic bending wavenumber were adjusted at fixed values of the spin−orbit coupling constant A_0 and the Renner parameter ϵ. After an unambiguous assignment of the first Fermi polyads was made, a forward calculation of the next polyads was performed and compared to the spectrum. As the number of assigned lines became larger, the number of parameters to be adjusted was

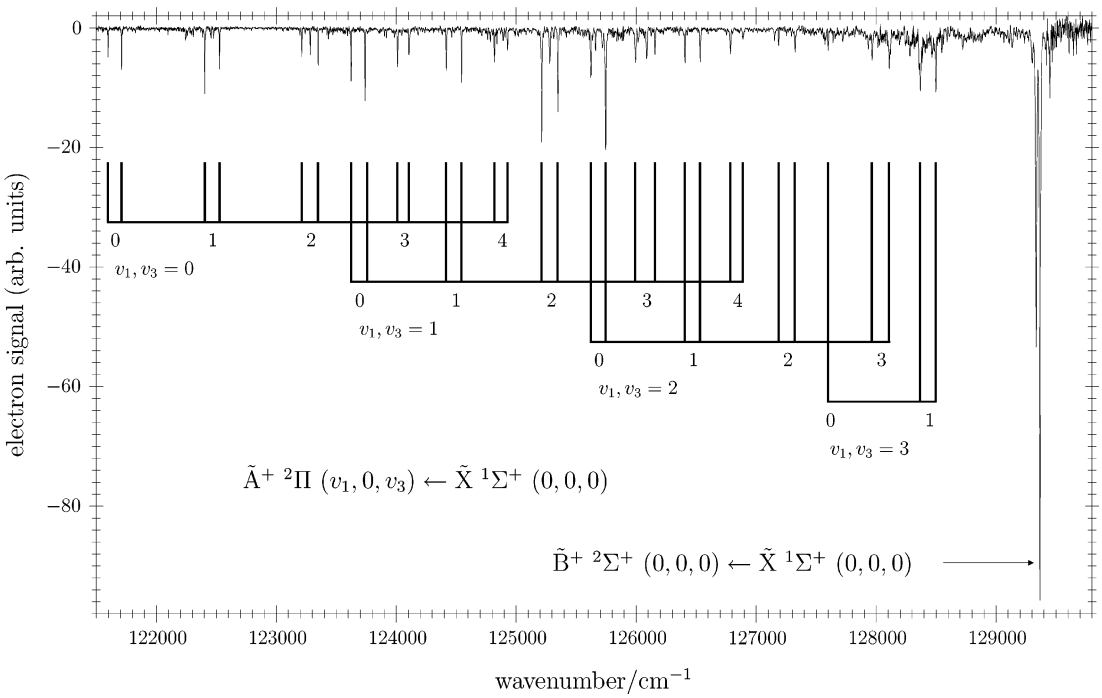

Figure 2. PFI-ZEKE photoelectron spectrum of OCS in the region of the $\tilde{X}\ ^1\Sigma^+ \rightarrow \tilde{A}^+\ ^2\Pi$ and $\tilde{X}\ ^1\Sigma^+ \rightarrow \tilde{B}^+\ ^2\Sigma^+$ bands. The assignment bars indicate four vibrational progressions in the CS-stretching mode (ν_1) associated with excitation of up to three quanta ($\nu_3 = 0-3$) in the CO-stretching mode (ν_3). Each vibrational band shows two main components, corresponding to the two spin−orbit components of the $^2\Pi_\Omega$ state with $\Omega = {}^3/_2$ and ${}^1/_2$. In the higher members of the progressions, the Fermi interactions lead to additional structures.

increased until most observed lines of the first five polyads could be unambiguously attributed. Several weak features in Figures 3 and 4 were at the limit of the detection sensitivity of the measurement and were not used in the fitting procedure, which we restricted to the stronger lines.

In the final phase of the analysis, molecular parameters were determined for both progressions in a nonlinear least-squares-fitting procedure, the results of which are summarized in Table 1. A total of nine parameters could be determined for each progression, including the following: the ionization energy (IE), the bending and CS-stretching wavenumbers ($\omega_2^{(0)}$, $\omega_2^{(1)}$ and $\omega_1^{(0)}$, $\omega_1^{(1)}$; see eqs 18−21), the anharmonic constant (x_{11}), the Renner−Teller parameter ϵ, the spin−orbit constants A_0 and α_1, and the Fermi coupling parameters W_1 and W_2. IE corresponds to the transition from the $\tilde{X}\ ^1\Sigma^+(0, 0, 0)$ vibronic ground state to the $\tilde{A}^+\ ^2\Pi_{3/2}(0, 0, 0)$ and $\tilde{A}^+\ ^2\Pi_{3/2}(0, 0, 1)$ states; in the case of the $\nu_3 = 0$ progression, IE corresponds to the adiabatic ionization energy. In addition, the constants $\omega_3^{(0)}$ (see eq 22) and x_{33} could be derived from the positions of the first members of the $(0,0,\nu_3)$ progression. The root-mean-square (rms) deviations of the fits were 2.2 and 1.3 cm^{-1} for the $\nu_1 = 0$ and $\nu_1 = 1$ progressions, respectively. The observed and calculated positions of the members of the $\nu_3 = 0$ and $\nu_3 = 1$ progressions are compared in Tables 2 and 3, respectively. These tables list the positions of all levels of the polyads with $\nu_p \leq 2$ but only the observed levels in higher polyads. The maximal deviations between calculated and experimental wavenumbers were 4.6 cm^{-1} ($\nu_3 = 0$ progression) and 2.5 cm^{-1} ($\nu_3 = 1$ progression). Given that the width of the observed bands was ∼5 cm^{-1}, the agreement between calculation and experiment can be regarded as satisfactory. The harmonic wavenumbers ω_1, ω_2, and ω_3 and the anharmonicity constants x_{13} and x_{23} that can be derived from the results of the fits using eqs 18−22 are listed in the lower portion of Table 1.

The validity of the assignments made in the present investigation are supported by the following two observations. First, the

TABLE 1: Results of Least-Squares Fits of the Molecular Parameters Used to Describe the Renner−Teller Effect in the $\tilde{A}^+\ ^2\Pi$ State of OCS$^+$ with the Model Described in Section 3,[a] and Harmonic Frequencies and Anharmonicity Constants Determined from the Results of the Fit and the Positions of the First Members of the (0,0,ν_3) Progression ($\nu_3 \leq 2$)[b]

	Value	
parameter	$\nu_3 = 0$	$\nu_3 = 1$
Results of Least-Squares Fits		
IE/(hc) (cm^{-1})	121598.8(20)[c]	123624.8(30)
$\omega_2^{(0)}$, $\omega_2^{(1)}$ (cm^{-1})	353.5(20)[d]	346.0(43)
ϵ	−0.225(10)[e]	−0.210(18)
A_0 (cm^{-1})	−114.5(20)[f]	−116.3(14)
α_1 (cm^{-1})	1.0(36)	2.1(17)
$\omega_1^{(0)}$, $\omega_1^{(1)}$ (cm^{-1})	805.4(55)[g]	797.7(18)
x_{11} (cm^{-1})	−0.8(13)	−2.4(3)
W_1 (cm^{-1})	16.5(11)	17.0(12)
W_2 (cm^{-1})	0.2(7)	0.7(6)
Harmonic Frequencies and Anharmonicity Constants		
ω_1 (cm^{-1})	809(6)	
ω_2 (cm^{-1})	357(5)	
ω_3 (cm^{-1})	2062(5)	
x_{12} (cm^{-1})	0	
x_{13} (cm^{-1})	−7.7(60)	
x_{23} (cm^{-1})	−7.5(50)	
x_{33} (cm^{-1})	−12(3)	

[a] The root-mean-square deviation of the fits were 2.2 and 1.3 cm^{-1} for the progressions associated with $\nu_3 = 0$ and $\nu_3 = 1$, respectively. [b] The numbers in parentheses represent one standard deviation. [c] The adiabatic ionization energy is given as 121595 ± 4 cm^{-1} in ref 14. [d] A value of 417 cm^{-1} can be derived using $\omega_2 = \sqrt{(1/2)(\omega_{2,A'}^2+\omega_{2,A''}^2)}$ and the theoretical values for $\omega_{2,A'}$ and $\omega_{2,A''}$ given in Table 1 of ref 14. [e] A value of $\epsilon = -0.2137$ can be derived using $\epsilon = (\omega_{2,A'}^2 - \omega_{2,A''}^2)/(\omega_{2,A'}^2 + \omega_{2,A''}^2)$ and the theoretical values for $\omega_{2,A'}$ and $\omega_{2,A''}$ given in Table 1 of ref 14. [f] An experimental value of 114 cm^{-1} is given in ref 14. [g] A theoretical value of 812.6 cm^{-1} is given in Table 1 of ref 14.

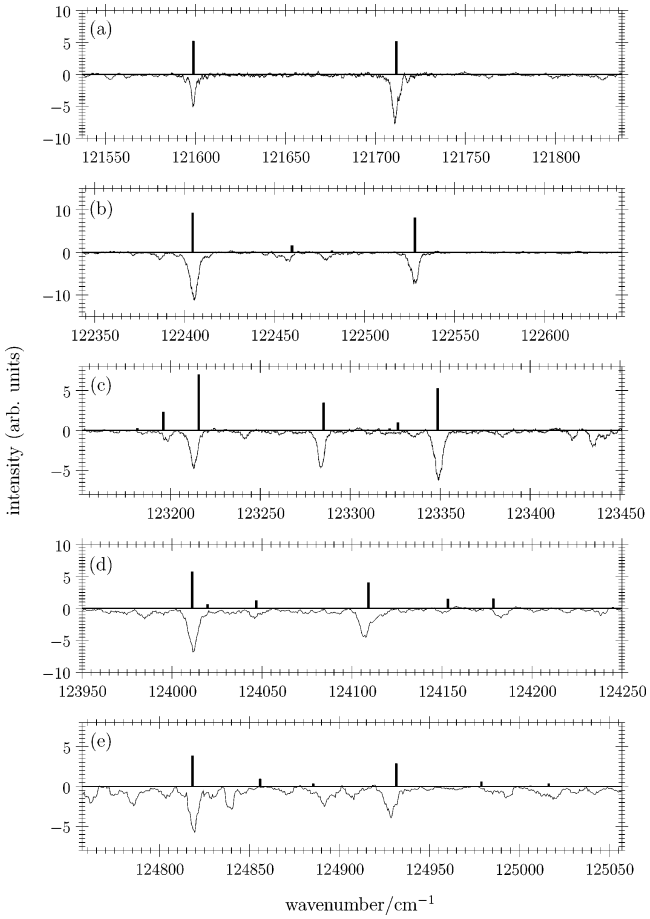

Figure 3. Details of the PFI-ZEKE photoelectron spectrum of OCS in the region of the successive Fermi polyads clustering around the CS-stretching levels with (a) $v_1 = 0$, (b) $v_1 = 1$, (c) $v_1 = 2$, (d) $v_1 = 3$, and (e) $v_1 = 4$. The spectra correspond to the vibrational progression associated with $v_3 = 0$. In each panel, the inverted traces correspond to the experimental spectra and the stick spectra to the results of calculations including the Renner−Teller effect and the spin−orbit and Fermi interactions.

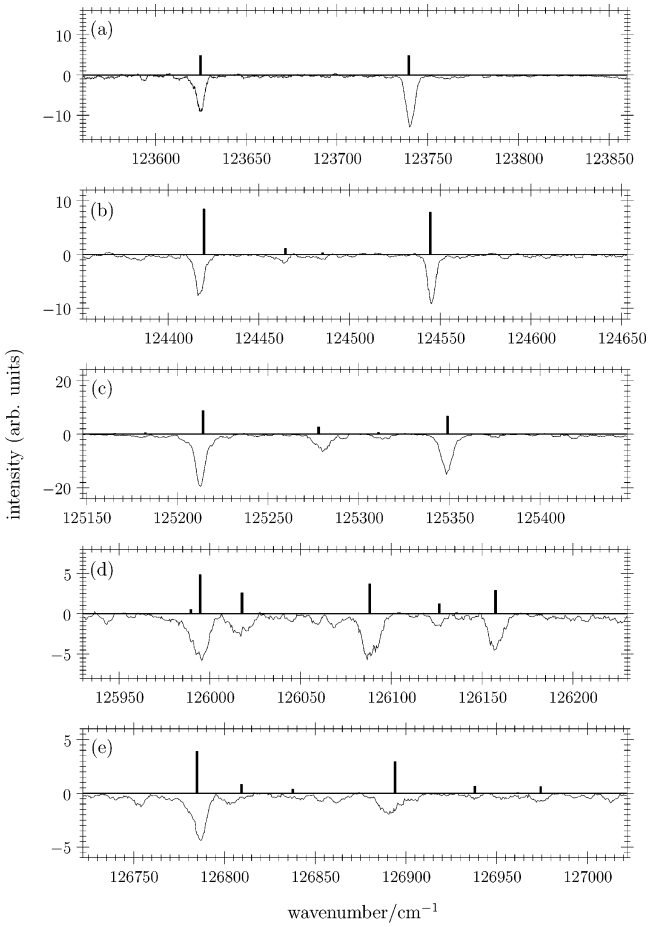

Figure 4. Details of the PFI-ZEKE photoelectron spectrum of OCS in the region of the successive Fermi polyads clustering around the CS-stretching levels with (a) $v_1 = 0$, (b) $v_1 = 1$, (c) $v_1 = 2$, (d) $v_1 = 3$, and (e) $v_1 = 4$. The spectra correspond to the vibrational progression associated with $v_3 = 1$. In each panel, the inverted traces correspond to the experimental spectra, and the stick spectra to the results of calculations including the Renner−Teller effect and the spin−orbit and Fermi interactions.

independent fits of the two vibrational progressions yielded very similar sets of molecular parameters, in accordance with the expected weak dependence of the molecular parameters on the excitation of the ν_3 mode (see, e.g., eqs 18−21). Second, the stretching character of the eigenstates could be used to successfully account for the intensity distribution of the photoelectron spectra.

To obtain a qualitative understanding of the intensity distribution in the PFI-ZEKE photoelectron spectrum, the spectrum was simulated by exploiting both the eigenvalues and the eigenvectors of the effective Hamiltonian (see eq 2). The eigenvalues were used to determine the positions of the lines in the PFI-ZEKE photoelectron spectrum, and the eigenvectors were used to estimate the relative line intensities. To this end, the following approximations were made: (i) it was assumed that the intensity of the transitions is solely carried by the stretching modes ν_1 and ν_3, the transitions to the bending levels being either vibronically forbidden or associated with vanishing Franck−Condon factors; (ii) the relative intensities of the lines were calculated as sums of products of the square of the stretching coefficients, with the Franck−Condon factors associated with transitions to the different stretching levels; and (iii) the Franck−Condon factors were themselves estimated from the relative intensities of the He I photoelectron spectra.[4,5,8] Despite the approximate nature of this treatment, the intensity calculations turned out to reproduce the main aspects of the intensity distributions, as is illustrated in Figures 3 and 4, which compare the experimental spectra (lower inverted traces in each panel) with the simulated spectra (displayed as stick spectra) for the two main stretching progressions.

Although our attribution of the two main components of each polyad to the two spin−orbit components ($^2\Pi_{3/2}$ and $^2\Pi_{1/2}$) of the CS-stretching levels is in good agreement with the results of the recent analysis of Chen et al.[14] (see their Table 2 for the results of theoretical predictions and their Table 3 for a summary of their experimental assignments), our analysis leads to very different assignments for the weaker members of the Fermi polyads. The main reason for the differences in the assignments lies in the very different values of the bending frequency determined in the two studies. Whereas a value of $\sim$350 cm^{-1} was determined in our analysis (see Table 1), the attributions in ref 14 rely on a value of 417 cm^{-1} (as determined from the average values of the bending frequencies of the two Renner−Teller potential curves; see footnote d in Table 1). This large discrepancy has a profound effect on the assignments: In our analysis, the bending frequency is observed to be less than half the CS-stretching frequency and the dominant Fermi interactions are between the highest components of the bending polyads (labeled κ in Figure 1) and the stretching levels, whereas, in the analysis of Chen et al., the bending frequency is more than

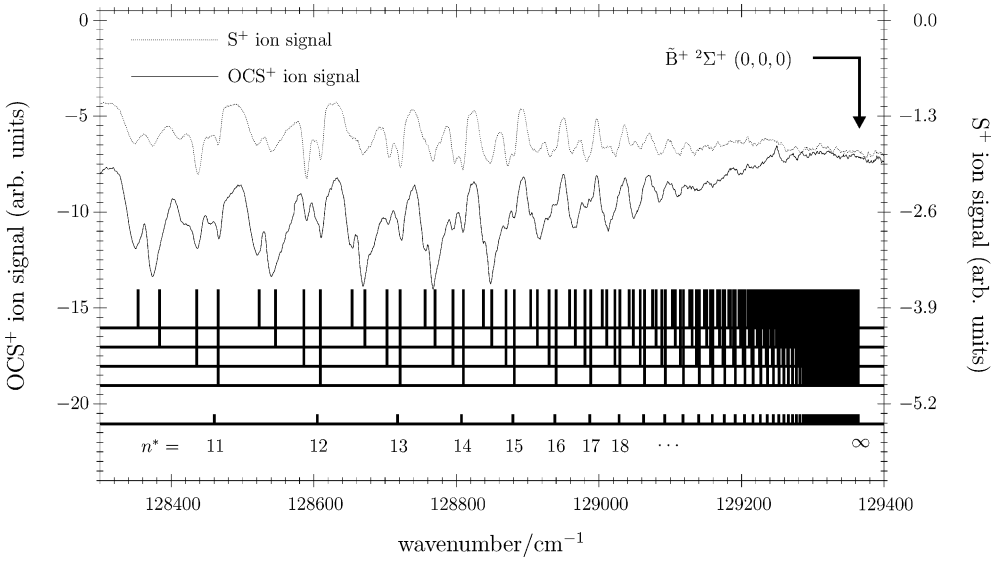

Figure 5. Photoionization spectrum of OCS below the $\tilde{X}\ ^1\Sigma^+ \rightarrow \tilde{B}^+\ ^2\Sigma^+$ ionization threshold. The spectrum consists of several Rydberg series that converge on the vibrational ground level of the $\tilde{B}^+\ ^2\Sigma^+$ state and are visible both in the photoionization (OCS^+) and the dissociative ionization (S^+) channels.

TABLE 2: Experimental and Calculated Positions of the Vibrational Energy Levels of the $\tilde{A}^+\ ^2\Pi$ State of OCS^+ Corresponding to the Progression Associated with $v_3 = 0$[a]

Assignment			$E/(hc)$ (cm^{-1})		CS-stretching character[c]
symmetry	v_p	(v_1,v_2,v_3)[b]	observed	calculated	
$^2\Pi_{3/2}$	0	(0,0,0)	121598.8	121598.8	0.99
$^2\Pi_{1/2}$	0	(0,0,0)	121710.9	121711.6	0.99
$\mu^2\Sigma_{1/2}$	1	(0,1,0)		121904.1	0.00
$^2\Delta_{5/2}$	1	(0,1,0)		121938.8	0.00
$^2\Delta_{3/2}$	1	(0,1,0)		122048.2	0.00
$\kappa^2\Sigma_{1/2}$	1	(0,1,0)		122103.1	0.00
$\mu^2\Pi_{3/2}$	2	(0,2,0)		122207.7	0.03
$\mu^2\Pi_{1/2}$	2	(0,2,0)		122217.7	0.02
$^2\Phi_{7/2}$	2	(0,2,0)		122271.1	0.00
$^2\Phi_{5/2}$	2	(0,2,0)		122375.4	0.00
$^2\Pi_{3/2}$	2	(1,0,0)	122404.9	122404.4	0.94
$\kappa^2\Pi_{1/2}$	2	(0,2,0)	122457.3	122459.7	0.16
$\kappa^2\Pi_{3/2}$	2	(0,2,0)	122478.1	122481.9	0.03
$^2\Pi_{1/2}$	2	(1,0,0)	122528.0	122528.0	0.83
$\kappa^2\Pi_{3/2}$	4	(0,4,0), (1,2,0)	123198.9	123196.2	0.22
$^2\Pi_{3/2}$	4	(2,0,0)	123213.0	123215.8	0.70
$\kappa^2\Pi_{1/2}$	4	(1,2,0), (2,0,0)	123283.7	123285.2	0.34
$^2\Pi_{1/2}$	4	(2,0,0), (1,2,0)	123348.9	123348.6	0.52
$^2\Pi_{3/2}$	6	(3,0,0)	124011.6	124011.1	0.74
$\kappa^2\Pi_{1/2}$	6	(2,2,0), (0,6,0)	*d*	124019.7	0.08
$\kappa^2\Pi_{3/2}$	6	(2,2,0), (0,6,0)	124045.8	124046.8	0.15
$^2\Pi_{1/2}$	6	(3,0,0)	124109.1	124109.2	0.52
$\kappa^2\Pi_{1/2}$	6	(1,4,0), (2,2,0)	124183.2	124178.6	0.19
$^2\Pi_{3/2}$	8	(4,0,0)	124818.3	124818.3	0.79
$^2\Pi_{1/2}$	8	(4,0,0)	124928.9	124931.6	0.58

[a] This table lists all calculated levels up to the second Fermi polyad ($v_p = 2$). For higher polyads, only the levels observed experimentally are listed. The calculations were made using the molecular parameters describing the Renner−Teller effect and spin−orbit and Fermi interactions listed in Table 1. [b] Main components. [c] CS-stretching character of each level used to determine the intensities. [d] Shoulder.

TABLE 3: Experimental and Calculated Positions of the Vibrational Energy Levels of the $\tilde{A}^+\ ^2\Pi$ State of OCS^+ Corresponding to the Progression Associated with $v_3 = 1$[a]

Assignment			$E/(hc)$ (cm^{-1})		CS-stretching character[c]
symmetry	v_p	(v_1,v_2,v_3)[b]	observed	calculated	
$^2\Pi_{3/2}$	0	(0,0,1)	123624.8	123624.8	1.00
$^2\Pi_{1/2}$	0	(0,0,1)	123740.3	123739.6	0.99
$\mu^2\Sigma_{1/2}$	1	(0,1,1)		123927.7	0.00
$^2\Delta_{5/2}$	1	(0,1,1)		123957.9	0.00
$^2\Delta_{3/2}$	1	(0,1,1)		124069.6	0.00
$\kappa^2\Sigma_{1/2}$	1	(0,1,1)		124117.3	0.00
$\mu^2\Pi_{3/2}$	2	(0,2,1)		124225.3	0.03
$\mu^2\Pi_{1/2}$	2	(0,2,1)		124235.5	0.02
$^2\Phi_{7/2}$	2	(0,2,1)		124283.6	0.00
$^2\Phi_{5/2}$	2	(0,2,1)		124390.4	0.00
$^2\Pi_{3/2}$	2	(1,0,1)	124417.3	124419.7	0.93
$\kappa^2\Pi_{1/2}$	2	(0,2,1)	124464.4	124464.6	0.12
$\kappa^2\Pi_{3/2}$	2	(0,2,1)	124485.2	124485.1	0.03
$^2\Pi_{1/2}$	2	(1,0,1)	124545.0	124544.5	0.87
$^2\Pi_{3/2}$	4	(2,0,1)	125212.1	125214.2	0.86
$\kappa^2\Pi_{1/2}$	4	(1,2,1)	125280.4	125277.9	0.26
$^2\Pi_{1/2}$	4	(2,0,1)	125348.9	125348.0	0.65
$\kappa^2\Pi_{1/2}$	6	(2,2,1), (0,6,1)	*d*	125989.5	0.06
$^2\Pi_{3/2}$	6	(3,0,1)	125993.6	125994.6	0.56
$\kappa^2\Pi_{3/2}$	6	(3,0,1), (2,2,1)	126017.5	126017.7	0.30
$^2\Pi_{1/2}$	6	(3,0,1)	126088.7	126088.1	0.43
$\kappa^2\Pi_{1/2}$	6	(3,0,1), (2,2,1)	126157.9	126157.4	0.34
$\mu^2\Pi_{1/2}$	8	(1,6,1)	126125.5	126126.5	0.14
$^2\Pi_{3/2}$	8	(4,0,1)	126786.3	126784.8	0.74
$^2\Pi_{1/2}$	8	(4,0,1)	126891.5	126894.0	0.56

[a] The table lists all calculated levels up to the second Fermi polyad ($v_p = 2$). For higher polyads, only the levels observed experimentally are listed. The calculations were made using the molecular parameters describing the Renner−Teller effect and spin−orbit and Fermi interactions listed in Table 1. [b] Main components. [c] CS-stretching character of each level used to determine the intensities. [d] Shoulder.

half the CS-stretching wavenumber, leading to a rather different pattern of Fermi interactions. In the higher Fermi polyads, the differences between our results and those of ref 14 become so large that no common assignments can be found between the two studies. Note that the assignments proposed in Table 3 of ref 14 were made by establishing correspondences between calculated and measured positions and do not appear to have taken other sources of information, such as line intensities, into account. For instance, several lines are assigned to transitions from the $\tilde{X}^1\Sigma^+(000)$ ground state to bending levels of Σ^+ and Δ symmetry in Table 3 of ref 14. We have not observed these transitions in our spectra. The good agreement between the experimental and simulated spectra displayed in Figures 3 and 4 constitutes, in our opinion, a strong indication in favor of the present assignments, and the assignments proposed in ref 14 should be regarded as tentative assignments guided by numerical ab initio calculations.

4.2. The PFI-ZEKE Photoelectron Spectrum of the $\tilde{X} \rightarrow \tilde{B}^+$ Band. The PFI-ZEKE photoelectron spectrum of OCS shows two closely spaced lines, separated by ~30 cm^{-1}, near the expected origin of the $\tilde{X} \rightarrow \tilde{B}^+$ transition. The $\tilde{B}^+$ state is a $^2\Sigma^+$ state; therefore, this doublet structure cannot be explained by a fine structure splitting. In their previous investigation, Chen et al.[14] also noticed this doublet structure and attributed the upper component of the doublet to the origin of the $\tilde{X} \rightarrow \tilde{B}^+$ transition, on the basis of the results of earlier photoelectron spectroscopic studies, but did not discuss possible assignments of the lower component of the doublet.

The spectral structure observed in the photoionization spectrum provides a means to derive an unambiguous assignment of the origin of the $\tilde{X} \rightarrow \tilde{B}^+$ transition. The photoionization spectrum below the onset of the $\tilde{X} \rightarrow \tilde{B}^+$ transition is displayed in Figure 5 and reveals several Rydberg series observed both in the photoionization (OCS^+) and dissociative ionization (S^+) yield. These series all converge to the same ionic limit at 129367(5) cm^{-1} which exactly corresponds to the position of 129365.9(30) cm^{-1} of the upper of the two closely spaced lines in the PFI-ZEKE photoelectron spectrum, leaving no doubt that this upper line actually corresponds to the origin of the $\tilde{X} \rightarrow \tilde{B}^+$ transition. The observation of these series and the non-observation of series converging on the position of 129334.4(30) cm^{-1} of the lower of the two lines observed in the PFI-ZEKE photoelectron spectrum provide additional information on the assignment of this line in the PFI-ZEKE photoelectron spectrum. Indeed, one can rule out that this line corresponds to an ionic level that strongly interacts with the $\tilde{B}^+$ state, thereby gaining intensity in the photoelectron spectrum. If this were the case, one would have also observed Rydberg series converging on this level in the photoionization spectra, in contrast to the experimental results. Instead, one must conclude that this line corresponds to a transition to a vibrationally excited level of the $\tilde{A}^+$ state that gains intensity in the PFI-ZEKE photoelectron spectrum by a channel interaction with one or more Rydberg states belonging to series that converge to the $\tilde{B}^+(0,0,0)$ level.

5. Conclusions

A complete analysis of the vibrational structure and the intensity distribution of the PFI-ZEKE photoelectron spectrum of the $\tilde{X}\ ^1\Sigma^+ \rightarrow \tilde{A}^+\ ^2\Pi$ transition of OCS has been performed. This analysis has led to a characterization of the Renner−Teller effect, of the spin−orbit interaction, and of Fermi interactions between CS-stretching and bending levels in the $\tilde{A}^+\ ^2\Pi$ state of OCS^+. Although photoionizing transitions from the ground neutral state to the bending levels of the $\tilde{A}^+$ state are usually very weak, these transitions gain intensity from the transitions to the CS-stretching levels to which they are coupled via Fermi interactions. Information on the bending levels could be determined from the analysis of the perturbations of the CS-stretching levels.

The assignments of the bending levels of the $\tilde{A}^+$ of OCS^+ made in the present study differ markedly from assignments made recently in the analysis of the synchrotron PFI-ZEKE photoelectron spectrum of OCS.[14] The present results indicate that the harmonic bending wavenumber of OCS^+ is <360 cm^{-1}, whereas the assignments in ref 14 were based on a value of >400 cm^{-1}. This large discrepancy in the bending wavenumber leads to completely different energy-level patterns in the successive Fermi polyads.

Besides the derivation of a set of parameters (which are listed in Table 1) describing the vibronic structure of the $\tilde{A}^+$ state of OCS^+, the present investigation also led to the determination of improved values of 121598.8(20) cm^{-1} and 129365.9(30) cm^{-1} for the second and third adiabatic ionization energies of OCS, corresponding to the formation of the $\tilde{A}^+$ and $\tilde{B}^+$ states of OCS^+. By combining the second adiabatic ionization energy with the value $\tilde{\nu}_{00} = 31404.099(7)$ cm^{-1} of the origin of the $\tilde{A}^+ \leftarrow \tilde{X}^+$ transition determined by Ochsner et al.,[22] an improved value of 90194.7(20) cm^{-1} can be derived for the first adiabatic ionization energy of OCS.

Acknowledgment. This work is supported financially by the Swiss National Science Foundation and the ETH Zürich.

References and Notes

(1) Turner, D. W.; Baker, C.; Baker, A. D.; Brundle, C. R. *Molecular Photoelectron Spectroscopy. A Handbook of He 584 Å Spectra*; Wiley−Interscience: London, 1970.
(2) Natalis, P.; Delwiche, J.; Collin, J. E. *Faraday Discuss. Chem. Soc.* **1972**, *54*, 98.
(3) Frey, R.; Gotchev, B.; Peatman, W. B.; Pollak, H.; Schlag, E. W. *Int. J. Mass Spectrom. Ion Phys.* **1978**, *26*, 137.
(4) Delwiche, J.; Hubin-Franskin, M.-J.; Caprace, G.; Natalis, P.; Roy, D. *J. Electron Spectrosc. Relat. Phenom.* **1980**, *21*, 205.
(5) Potts, A. W.; Fattahallah, G. H. *J. Phys. B* **1980**, *13*, 2545.
(6) Kovač, B. *J. Chem. Phys.* **1983**, *78*, 1684.
(7) Baer, T.; Guyon, P. M. *J. Chem. Phys.* **1986**, *85*, 4765.
(8) Wang, L.-S.; Reutt, J. E.; Lee, Y. T.; Shirley, D. A. *J. Electron Spectrosc. Relat. Phenom.* **1988**, *47*, 167.
(9) Merkt, F.; Mackenzie, S. R.; Rednall, R. J.; Softley, T. P. *J. Chem. Phys.* **1993**, *99*, 8430.
(10) Wiedmann, R. T.; White, M. G.; Lefebvre-Brion, H.; Cossart-Magos, C. *J. Chem. Phys.* **1995**, *103*, 10417.
(11) Baltzer, P.; Chau, F. T.; Eland, J. H. D.; Karlsson, L.; Lundqvist, M.; Rostas, J.; Tam, K. Y.; Veenhuizen, H.; Wannberg, B. *J. Chem. Phys.* **1996**, *104*, 8922.
(12) Huang, J.-C.; Cheung, Y.-S.; Evans, M.; Liao, C.-X.; Ng, C. Y.; Hsu, C.-W.; Heimann, P.; Lefebvre-Brion, H.; Cossart-Magos, C. *J. Chem. Phys.* **1997**, *106*, 864.
(13) Stimson, S.; Evans, M.; Ng, C. Y.; Hsu, C.-W.; Heimann, P.; Destandau, C.; Chambaud, G.; Rosmus, P. *J. Chem. Phys.* **1998**, *108*, 6205.
(14) Chen, W.; Hochlaf, M.; Rosmus, P.; He, G. Z.; Ng, C. Y. *J. Chem. Phys.* **2002**, *116*, 5612.
(15) Rupper, P.; Merkt, F. *Rev. Sci. Instrum.* **2004**, *75*, 613.
(16) Gauyacq, D.; Larcher, C.; Rostas, J. *Can. J. Phys.* **1979**, *57*, 1634.
(17) Larcher, C.; Gauyacq, D.; Rostas, J. *J. Chim. Phys.* **1980**, *77*, 655.
(18) Sears, T. J. *Mol. Phys.* **1986**, *59*, 259.
(19) Frye, J. M.; Sears, T. J. *Mol. Phys.* **1987**, *62*, 919.
(20) Kakoschke, R.; Boesl, U.; Hermann, J.; Schlag, E. W. *Chem. Phys. Lett.* **1985**, *119*, 467.
(21) Weinkauf, R.; Boesl, U. *J. Chem. Phys.* **1994**, *101*, 8482.
(22) Ochsner, M.; Tsuji, M.; Maier, J. P. *Chem. Phys. Lett.* **1985**, *115*, 373.
(23) Tsuji, M.; Maier, J. P.; Obase, H.; Sekiya, H.; Nishimura, Y. *Chem. Phys. Lett.* **1987**, *137*, 421.
(24) Guyon, P. M.; Baer, T.; Nenner, I. *J. Chem. Phys.* **1983**, *78*, 3665.
(25) Hollenstein, U.; Seiler, R.; Schmutz, H.; Andrist, M.; Merkt, F. *J. Chem. Phys.* **2001**, *115*, 5461.
(26) Hubin-Franskin, M.-J.; Delwiche, J.; Guyon, P.-M.; Richard-Viard, M.; Lavollée, M.; Dutuit, O.; Robbe, J.-M.; Flament, J.-P. *Chem. Phys.* **1996**, *209*, 143.
(27) Merkt, F.; Osterwalder, A.; Seiler, R.; Signorell, R.; Palm, H.; Schmutz, H.; Gunzinger, R. *J. Phys. B* **1998**, *31*, 1705.
(28) Signorell, R.; Palm, H.; Merkt, F. *J. Chem. Phys.* **1997**, *106*, 6523.
(29) Signorell, R.; Merkt, F. In *The Role of Rydberg States in Spectroscopy and Photochemistry*; Sándorfy, C., Ed.; Kluwer: Dordrecht, The Netherlands, 1999; p 479.
(30) Herzberg, G. *Molecular Spectra and Molecular Structure—Electronic Spectra and Electronic Structure of Polyatomic Molecules*; Krieger: Malabar, FL, 1991; Vol. III.
(31) Brown, J. M.; Jørgensen, F. In *Advances in Chemical Physics*; Prigogine, I., Rice, S. A., Eds.; Wiley: New York, 1983; Volume LII, p 117.
(32) Gauyacq, D.; Jungen, Ch. *Mol. Phys.* **1980**, *41*, 383.
(33) Smith, T. C.; Smith, H.; Li, H.; Hostutler, D. A.; Clouthier, D. J.; Merer, A. J. *J. Chem. Phys.* **2001**, *114*, 725.
(34) Hougen, J. T. *J. Chem. Phys.* **1962**, *37*, 403.
(35) Merkt, F.; Softley, T. P. *Int. Rev. Phys. Chem.* **1993**, *12*, 205.